Pt nanoparticles embedded metal-organic framework nanosheets: A synergistic strategy towards bifunctional oxygen electrocatalysis

Zhangxun Xia[a], Jian Fang[b,c,**], Xiaoming Zhang[a], Linpeng Fan[c], Anders J. Barlow[d], Tong Lin[c], Suli Wang[a], Gordon G. Wallace[b,e], Gongquan Sun[a,*], Xungai Wang[b,c,**]

[a] Division of Fuel Cell & Battery, Dalian National Laboratory for Clean Energy, Dalian Institute of Chemical Physics, Chinese Academy of Sciences, Dalian 116023, China
[b] ARC Centre of Excellence for Electromaterials Science (ACES), Australia
[c] Deakin University, Institute for Frontier Materials, Geelong, VIC, 3216, Australia
[d] Centre for Materials and Surface Science and Department of Chemistry and Physics, La Trobe University, Melbourne, VIC, 3086, Australia
[e] Intelligent Polymer Research Institute, University of Wollongong, Northfields Avenue, Wollongong, NSW, 2522, Australia

ARTICLE INFO

ABSTRACT

To meet the increasing demands for highly active electrocatalysts towards oxygen reduction reaction (ORR) and oxygen evolution reaction (OER), here in this work, a new strategy of synergistic nano-architecture design based on Platinum nanoparticles (Pt NPs) and ultrathin two-dimensional (2D) metal-organic frameworks (MOFs) is developed for bifunctional electrochemical catalysts. Compared with commercial Pt/C and RuO_2 catalysts, remarkable enhancements in activity and durability of both oxygen reduction and oxygen evolution reactions are achieved on our PtNPs@MOFs composite materials, with one of the lowest over-potential gaps (E_{gap}) of 665 mV that has ever been reported. The tests on the assembled Zn-air batteries have revealed promising electrocatalytic performance and practical advantage of our new materials as air cathode catalyst. Both experimental results and theoretical study have confirmed the synergistic effect between Pt NPs and MOF nanosheets through a "win-win" electron structural modification, demonstrating the effectiveness of our strategy in developing effective bifunctional oxygen electrocatalysts for various types of electrochemical devices.

1. Introduction

Among the electrochemical reactions related to sustainable energy conversion and storage technologies, oxygen reduction reaction (ORR) and oxygen evolution reaction (OER) are at the central place of many renewable energy devices such as fuel cells, metal-air batteries, and water splitting units [1–3]. Bifunctional electrocatalyst with both ORR and OER could be crucial for advanced energy devices like rechargeable Zn-air batteries, by combining both reactions on a single electrode [4–8]. Precious metals (such as platinum) and metal oxides (such as iridium oxide or ruthenium oxide) have been widely used as the electrocatalysts for ORR and OER, respectively [9–11]. However, neither of ORR and OER active materials can have sufficient catalytic activity towards the other reaction. Non-precious metal oxide and hydroxide materials also possess outstanding OER and ORR activity with significantly reduced cost compared to precious metals [12–15]. So far, low electrical conductivity and poor durability in some harsh electrochemical environments have limited their potential in practical

applications. Carbon based nanomaterials with nitrogen and/or metal doping exhibit promising bifunctional electrocatalytic performance because of their highly dispersed active sites, large surface area with an open porous structure and high electronic conductivity [8,16–19]. However, carbon corrosion that occurs at the ultra-positive potentials (0.5–2.0 V vs. RHE) during OER and ORR cycles would seriously shorten the lifetime of such materials. Although great efforts have been made in developing advanced electrocatalysts to improve either ORR or OER performance, it is still challenging to achieve narrow over-potential gap between ORR and OER on a single electrochemical catalyst and electrode. In this regard, novel materials with tailored structure and activity are desirable to meet the requirement of bifunctional electrocatalysis for various types of electrochemical devices.

Metal-organic frameworks (MOFs) are a group of microporous materials [20,21] that have been intensively developed in the last two decades for their promising applications in gas storage/separation [22,23], drug delivery [24,25], bio-imaging [26,27], sensing [28], and catalysis [29,30]. Formed by metal atom nodes and organic ligands via

coordinate bonds, the periodic and porous structure of MOFs leads to ultra-high surface areas, abundant active sites, and accessible transport pathways [31–34]. However, most reported MOFs applied as electrochemical catalysts still suffer from insufficient electronic conductivity, low utilization of active atoms, and unsmooth mass transport resulted from their structural nature. More recent developments in calcining MOFs to form a microporous carbon structure or metal alloy hold promise for enhanced electrochemical performance, but the uncontrollable size of the active sites during MOF thermal decomposition and poor durability remain as unsolved challenges [35–37]. In recent studies, new MOF materials with an ultrathin structure have demonstrated outstanding catalytic and separation performance in energy and electrochemical applications [38–40]. The unique 2D structure remarkably eliminates the blockages for electron and mass transport, whereas the utilization of active sites is largely enhanced via the high-level exposure of metal nodes in unsaturated coordination positions. In spite of the excellent OER performance that has been reported on ultrathin MOF nanosheets without any thermal treatment [39], such a dedicated design of singular MOF materials is far from satisfying in electrochemical applications requiring bifunctional OER and ORR catalysis.

Making composite materials containing metal nanoparticles (NPs) on or in MOF structures has been widely studied as an effective strategy to achieve new functions that are hardly realized by any individual material [41–43]. The highly porous structure, abundant options of organic ligands, and versatile fabrication procedures of MOFs have benefited the effective incorporation of various types of nanoparticles, through template formation of nanoparticles within MOF channels or encapsulation of pre-synthesized nanoparticles [41]. The NP/MOF composite materials have shown encouraging enhancement in catalytic effect in a wide range of electrochemical reactions, such as ORR [44,45], OER [46,47], hydrogen evolution reaction (HER) [48], alcohol oxidation reaction [49,50], and carbon dioxide reduction [51,52]. However, the reciprocal decoration effect between nanoparticles and ultrathin MOF sheets on oxygen electrocatalysis has not yet been fully explored.

Herein, a class of composite nanomaterials based on platinum NPs embedded in ultrathin 2D MOF nanosheets are designed and synthesized. General synergistic effects of Pt NPs and MOFs in this composite are found to boost OER on MOFs and ORR on Pt NPs from the electron decoration between Pt and metal nodes in MOFs. With the reciprocal modification effect, remarkable enhancement of catalytic activity and stability towards ORR and OER is achieved, and the potential gap can be significantly narrowed compared to the commercial catalysts and most of state-of-the-art bifunctional catalysts. The assembled Zn-air batteries showed promising electrochemical performance. Theoretical study further demonstrates that embedding highly active electrocatalytic NPs onto MOF nanosheets with the intrinsic mechanisms of the electron modification between NPs and MOFs can be a new strategy for bifunctional catalysis applications.

2. Materials and methods

2.1. Catalyst synthesis

2.1.1. Synthesis of Pt NPs

Platinum NPs were synthesized via ethylene glycol (EG) reduction method [53]. Briefly, 26.6 mg chloroplatinic acid (Sigma-Aldrich) was dissolved in 10 mL EG solution. After a constant stirring for 30 min, sodium hydroxide was then added to the solution to adjust the pH value as 12–13. Then the solution was kept at 130 °C in an oil bath with constant stirring for 4 h. After cooling down to room temperature, the Pt NPs colloid was prepared with a Pt concentration of 1 mg mL^{-1}.

2.1.2. Synthesis of MOF nanosheets and bulk MOF particles

MOF samples were synthesized based on the method proposed by

previous reports [38,39,54]. Typically, 0.2 mmol terephthalic acid (98%, Sigma-Aldrich) was dissolved in 10 mL mixture solution (8 mL DMF, 0.5 mL ethanol, and 0.5 mL de-ionized water), and then 0.3 mmol metal salt was added to the above solution. 0.2 mL triethylamine was then quickly added to the mixture solution, and the container was sealed and kept under constant ultra-sonication with a power of 200 W for 6 h. The as-prepared mixture slurry was then centrifuged at 5000 rpm, and washed by ethanol for 4 times. After drying in a vacuum oven at 60 °C, the MOF nanosheets were prepared for further analyses. The above mentioned metal salt referred to one of $NiCl_2 \cdot 6H_2O$, $CoCl_2 \cdot 6H_2O$, $CuCl_2 \cdot 3H_2O$, and $FeCl_2 \cdot 4H_2O$, and the as-prepared MOFs samples were denoted as NiNSMOFs, CoNSMOFs, CuNSMOFs, and FeNSMOFs, respectively. Unlike the MOF nanosheets formed during the ultra-sonication process, the bulk MOF samples were prepared only with constant stirring at room temperature, using exactly the same starting materials and concentrations.

2.1.3. Synthesis of Pt@NSMOFs

First, 0.2 mmol terephthalic acid (98%, Sigma-Aldrich) was dissolved in 10 mL mixture solution (8 mL DMF, 0.5 mL ethanol, and 0.5 mL de-ionized water), and then 0.3 mmol metal salt was added to the above solution. A certain volume of Pt colloid was then added to the solution with a constant stirring for 8 h. 0.2 mL triethylamine was quickly added to the mixture solution, and the container was sealed and kept under constant ultra-sonication with a power of 200 W for 6 h. The as-prepared mixture slurry was then centrifuged at 5000 rpm, and washed by ethanol for 4 times. After dried in vacuum oven at 60 °C, the composite nanosheet samples were prepared for further analyses. The volume of Pt colloid added in the DMF solution was 0.2, 0.4, 1, and 2 mL, which roughly equivalent to Pt weight content in the composite materials as 0.7, 2.0, 3.2, and 8.8 wt.%. The corresponding composite nanosheetsamples were denoted as Pt0.7%@NSMOFs, Pt2.0%@ NSMOFs, Pt3.2%@NSMOFs, and Pt8.8%@NSMOFs, respectively. The photographs of the samples at different preparation stages are shown in Fig. S1.

2.2. Characterizations of materials

X-ray diffraction (XRD, X'pert MRD XL) spectrascopy has been used to investigate the crystal sturcure of the materaials. XRD patterns of NiMOF nanosheets, bulk NiMOF particles and Pt3.2%@NiNSMOFs were recorded on a Panalytical X-ray diffractometer using Cu radiation of 1.54 Å. The samples were scanned in the 2θ range of 5°–60° with a step size of 0.05°. Field emission scanning electron microscopy (FE-SEM, Supra 55 V P, Zeiss) was used to exmaine the morphology of differnt MOF materials. High resolution TEM (HRTEM), selected area electron diffraction (SAED), energy dispersive X-ray (EDX) spectra and mapping were obtained on a JOEL FEG 2100 F TEM at anaccelerating voltage of 200 kV. Atomic force microscopic (AFM) results were obtained using a Bruker MultiMode 8 AFM in ScanAsyst-Air mode with a ScanAsyst-Air Silicon Nitride probe (Bruker, Australia).

N_2 adsorption isotherms were performed at 77.4 K using a Quantachrome NOVA 2200e instrument. Before analysis, the samples were out-gassed at 200 °C under vacuum for 6 h. The specific surface areas were calculated using adsorption data by the Multi-Point Brunauer-Emmett-Teller (BET) method. The thermal decomposition behavior of the materials was investigated by thermogravimetry analysis (TGA) and differential thermal analysis (DTA) performed on a TG analyzer (Q600, TA Instruments) at a heating rate of 10 °C min^{-1} from 25 to 700 °C in air. Temperature-programmed reduction with hydrogen (H_2-TPR, with 5 vol.% H_2 in Ar) and chemisorption with pulse CO (5 vol.% CO in He) were carried out with an autochemisorption instrument (ChemBET Pulsar, Quantachrome) equipped with a thermal conductivity detector (TCD). For TPR tests, a ramp rate of 10 °C min^{-1} and a temperature range between 25–600 °C were used for all the experiments. For pulse chemisorption tests, all samples were thermally

pre-treated at 150 °C to remove any possible surface contamination. All adsorption processes in pulse chemisorption were carried out at -80 ± 5 °C by keeping the reactor in a bath of isopropanol and liquid nitrogen.

The X-ray photoelectron spectroscopy (XPS) analyses were performed using a Kratos Analytical AXIS Nova spectrometer (Manchester, UK) equipped with a monochromatic Al KαX-ray source (1486.69 eV). High-resolution elemental analyses were performed on C 1s (295–275 eV), Ni 2p (850–885 eV), Co 2p (775–810 eV), and Pt 4f (84–64 eV) regions with a npass energy of 20 eV, a 0.1 eV step and a 250 ms dwell time. Each spectrum was constructed from an average of 25 scans for the Ni, Co and Pt regions. The pressure in the XPS analysis chamber was maintained at 1×10^{-8} mbar or lower during collection. Charge neutralisation was used throughout the analysis and in the data analysis the binding energy (BE) of the core level C 1s peak was set at 284.5 eV to compensate for surface-charging effects. The Shirley background was subtracted, and the satellite peaks were removed for all element peaks before curve fitting. The experimental spectra were fitted into components of a Gaussian line shape.

2.3. Electrochemical characterizations

The electrochemical characterizations were conducted in a three-electrode cell with a CHI 760D potentiostat/galvanostat at room temperature (298 K). 2.5 mg as-prepared samples were mixed with the same weight of carbon powder (Vulcan XC 72, Carbot), 0.02 mL of Nafion dispersion (5 wt.% in water, Sigma-Aldrich), and 2 mL ethanol to form a catalyst ink, and then drop coated on a rotation ring disk electrode (RRDE) with a typical catalyst sample loading of 0.1 mg cm^{-2}. During the test, 0.1 M KOH solution, a Ag/AgCl electrode, and a Pt wire was used as electrolyte, reference electrode (RE) and counter electrode (CE), respectively. The measured potentials (vs. Ag/AgCl) were converted to a reversible hydrogen electrode (RHE) using Nernst equation. Cyclic voltammetry (CV) between 0 and 1.2 V vs. RHE at a scan rate of 50 mV s^{-1} was performed under the continuous purging of high purity N$_2$. ORR polarization curves were obtained by CV tests between 0 and 1.2 V vs. RHE at a scan rate of 10 mV s^{-1} in oxygen saturated electrolyte. The electron transfer numbers can be calculated with Koutecky–Levich equations:

$$\frac{1}{j}=\frac{1}{j_L}+\frac{1}{j_K}=\frac{1}{B\omega^{\frac{1}{2}}}+\frac{1}{j_K} \tag{1}$$

$$B=0.62nFC_0(D_0)^{2/3}\nu^{-1/6} \tag{2}$$

$$j_K=nFkC_0 \tag{3}$$

where j$_K$, j$_L$, and j are the kinetic, diffusion-limiting and the measured current densities, respectively; ω is the angular velocity of the disk; F refers to the Faraday constant (F = 96485 C mol^{-1}); n represents the overall number of electrons transferred in oxygen reduction; D$_0$ is thediffusion coefficient of O$_2$ in 0.1 M KOH electrolyte (1.9×10^{-5} cm^2 s^{-1}); C$_0$ means the bulkconcentration of O$_2$ (1.2×10^{-6} mol cm^{-3}); v is the kinematics viscosity of electrolyte, and k is theelectron-transferred rate constant.

OER polarization curves were obtained by CV tests between 1.0 and 1.8 V vs. RHE at a scan rate of 10 mV s^{-1} in oxygen saturated electrolyte. The accelerating stress tests (AST) were conducted via CV cycling between 0.6 and 1.2 V vs. RHE at a scan rate of 100 mV s^{-1} in N$_2$ saturated 0.1 M KOH electrolyte. The lifetime tests were performed on a piece of 0.5×1 cm^2 Ni foam loaded with 1 mg cm^{-2} as-prepared catalyst samples.

The total mass-based site density can be calculated from the CO pulse adsorption results by applying the following equation:

$$MSD_{total}=n_{CO} \times N_A \tag{4}$$

n_{CO} is the CO uptake obtained at -80 °C. N$_A$ is the Avogadro's constant

(6.022×10^{23} mol^{-1}). The mass-based site density for Pt NPs can be obtained from the electrochemical surface area (ECSA) calculated based on the hydrogen under-potential desorption (H-UPD) peaks by assuming a charge transfer of 210 μC cm^{-2} (2.1 C m^{-2})Pt surface:

$$ECSA=\frac{Q_H}{m_{Pt}\times 2.1} \tag{5}$$

$$MSD_{Pt\,NPs}=\frac{2.1}{F}\times ECSA\times N_A \tag{6}$$

Q_H is the integrated charge of the H-UPD from the CV curves. m_{Pt} is the Pt NPs mass loadings on the electrode. F is the Faraday's constant (96485.3 C mol^{-1}). The mass-based site density ascribing to MOFs (MSD$_{MOFs}$) can be obtained from MSD$_{total}$ substracted with MSD$_{Pt\,NPs}$. Turnover frequency (TOF) can be calculated by using the followed equation: [55]

$$TOF=\frac{I}{4F\times active\ site\ density} \tag{7}$$

I is the current density for ORR or OER at a given overpotential.

2.4. Zn-air battery tests

The rechargeable Zn-air batteries were assembled by using a commercial split test cell (MTI) with Zn powders as the anode, a cellulose film as the separator, and 6 M KOH + 0.2 M ZnCl$_2$ as the electrolyte solution. The air cathodes were fabricated by spraying a mixture of the as-prepared catalyst, carbon powder (Vulcan XC72, Carbot), and Nafion dispersion (5 wt.% in water, Sigma-Aldrich) dispersed in ethanol on the gas diffusion layer (GDL, 39BC, SGL) with a catalyst loading of 1 mg cm^{-2}. Polarization curves for charge and discharge were obtained using a battery test system (FCTS, Arbin) with air at room temperature. Electrochemical impedance spectroscopy (EIS) was obtained using Solartron SI1287 at a cell potential of 2.2 V for charge process and 1.0 V for discharge process. The spectra were collected in a frequency range of $0.1 - 10^5$ Hz with an amplitude of 5.0 mV.

2.5. DFT calculation

We carried out full geometry optimization with different geometries and spin states. The geometry with the lowest energy was regarded as the ground state and was considered for the further discussion. The detailed parameters can be found in the Supplementary Materials (Table S3). The DFT calculations for the intermediates forming on the Ni atom with Pt anchored for OER processes and Pt (111) surfaces with a unit group of MOFs absorbed for ORR processes were performed using the Vienna ab-initio simulation package (VASP). Projector augmented wave (PAW) method with generalized gradient approximation (GGA) of Perdew–Wang 1991 (PW91) was employed to describe valence-electron interactions. The detailed calculation processes of the intermediates for ORR and OER are described in the Supplementary Materials.

3. Results and discussion

3.1. Morphological and structural characterizations

Based on the structural design of the composite material, the Pt NPs are expected to be uniformly embedded on the MOF nanosheets surface, as schemed in Fig. 1a. The crystallographic details of the MOF nanosheets were characterized by X-ray diffraction (XRD), as shown in Fig. 1b. The characteristic peaks related to the MOF structure can be found among the range from 5° to 35°, which are consistent with the simulated pattern of the MOFs (blue line) and that of the similar MOFs structure reported in the literature. [39] Compared to the XRD pattern of bulk MOFs (Figs. S2 and S3), the peak located at about 9° indicates that the dominant facets on the MOF sheets surface should be the (200)
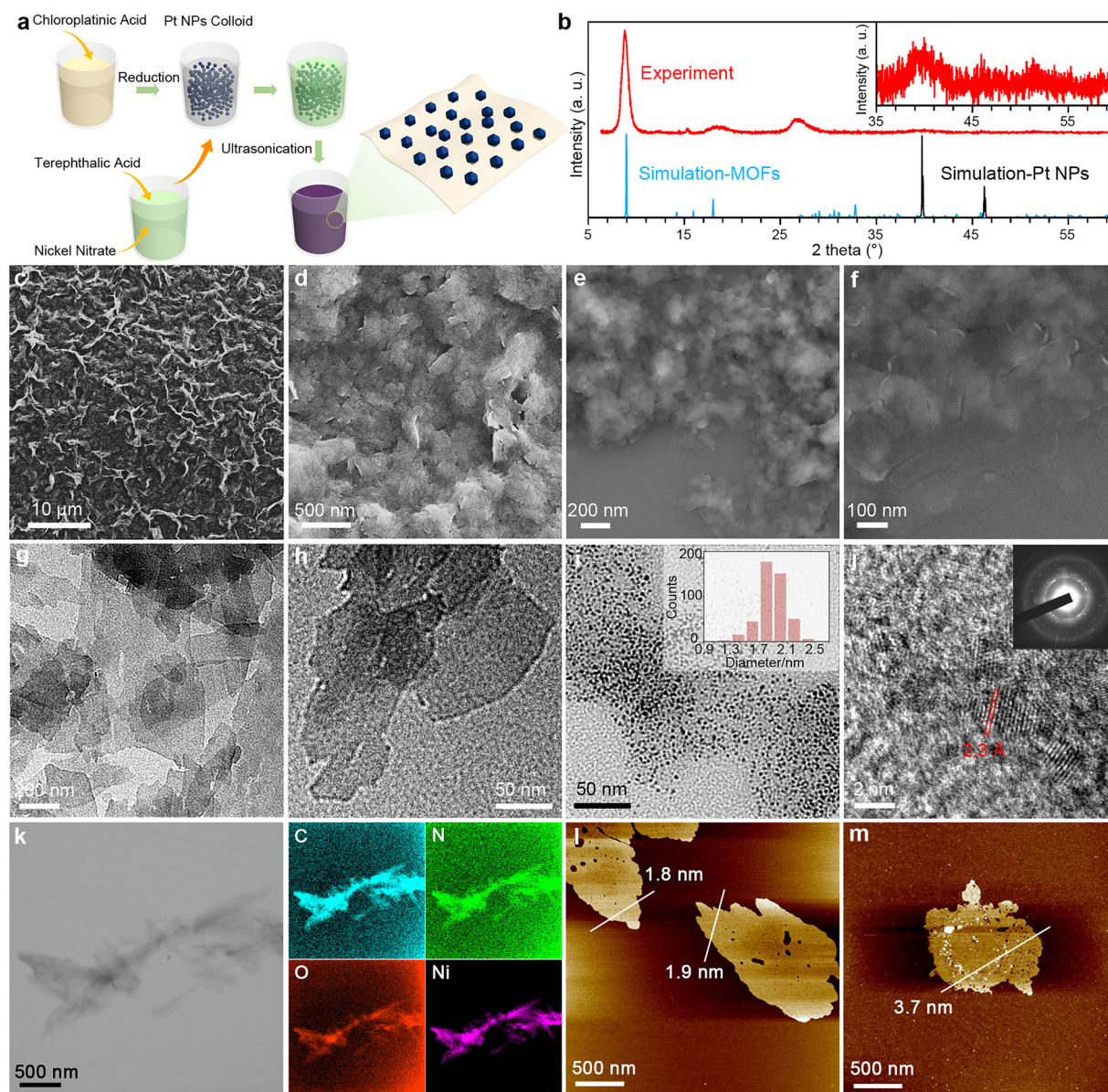
Fig. 1. (a) Schematic of the preparation procedures for Pt@NSMOFs; (b) Experimental and simulation XRD patterns of Pt@NiNSMOFs (scaled-up pattern is shown in the inset); (c–f) SEM images of NiNSMOFs; (g, h) TEM images of NiNSMOFs; (i, j) TEM images of Pt@NiNSMOFs (histogram of the Pt NPs size distribution and SAED patterns are shown in the insets of i and j, respectively); (k) EDX mapping results of NiNOMOFs; (l, m) AFM images of NiNSMOFs and Pt@NiNSMOFs.

facets with abundant unsaturated metal nodes, which could be catalytically active towards electrochemical reactions. Similar to the crystallographic characters of pure NiMOF nanosheets, Pt@NiNSMOFs also show predominating peak ascribed to the (200) facets of MOFs, as shown in Fig. 1b. Additionally, the peaks ascribed to Pt crystalline could be found in the pattern ranged from 35° to 60°, in which the peaks located at 40° and 46° are ascribed to Pt (111) and (110), respectively.

Surface morphology and microstructure of the samples were investigated by field emission scanning electron microscopy (FE-SEM) and transmission electron microscopy (TEM). The SEM image in Fig. 1c shows that a wrinkled structure can be formed by the stacking of pure NiMOF nanosheets. Separated pieces of pure NiMOF nanosheets are recognized in the SEM images with higher resolutions (Fig. 1d–f), and the average size of the nanosheets could be estimated as 0.9 ˜ 1.2 μm. TEM images reveal that the pure NiMOF nanosheets have the shape of irregular polygon (Fig. 1g, h), and the similar configuration has been maintained in Pt@NiNSMOFs samples embedded with Pt NPs (Fig. 1i). The Pt NPs are uniformly distributed on the nanosheets with an average

particle diameter of 1.9 nm (as shown in the inset diagram of Fig. 1i), which is consistent with the morphological details of the as-prepared Pt NPs (Fig. S4). Well defined crystallographic structure of Pt is indicated with the inter-planar distance of 2.3 Å, which is indexed to the lattice spacing of Pt (111) planes, as shown in Fig.1j and the inserted selected area electron diffraction (SAED) pattern. The elemental composition of NiNSMOFs could be revealed in the EDX mapping, as shown in Fig. 1k. The uniform distribution of C, N, O, and Ni further indicates the homogenous structure of the MOFs nanosheets. The ultrathin structure of the MOF samples has been confirmed by AFM characterization (Fig. 1l, m). The typical thickness of NiNSMOFs and Pt@NiNSMOFs is found as 1.9 and 3.7 nm respectively, which are consistent with the distance of two periodic unit cells of the MOFs (1.86 nm, Fig. S9). Similar surface and pore structures were further demonstrated in the bare MOFs sample and the Pt loaded MOFs, as shown in the N_2 sorption isotherms (Fig. S10a). Brunauer-Emmett-Teller (BET) surface areas of 101.5 and 109.2 $m^2 g^{-1}$ are calculated for NiNSMOFs and Pt3.2%@NiNSMOFs, respectively, with similar mesopore dominated pore size
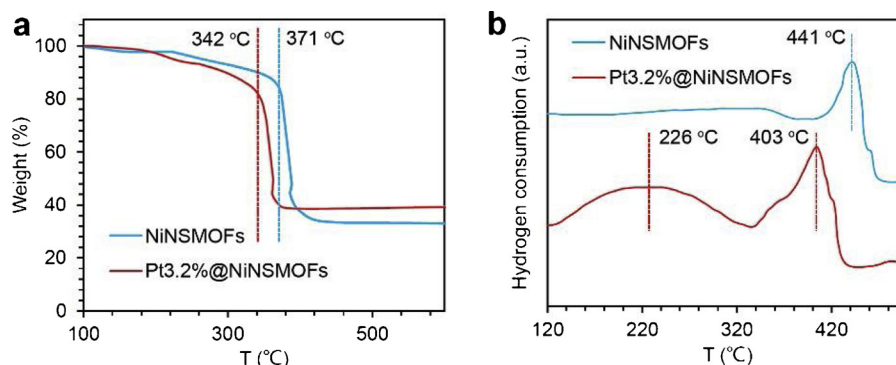
Fig. 2. (a) TGA curves and (b) H₂-TPR profiles for different samples.

distribution, as shown in Fig. S10b. Such feature could be derived from the stacking of the 2D nanosheets.

A weight loss of ca. 65% is observed from the TGA curve (Fig. 2a) for NiNSMOFs sample due to the thermal decomposition of MOFs at 371 °C. Smaller weight loss of ca. 60% is demonstrated for Pt3.2%@ NiNSMOFs for the loading of Pt. The thermal decomposition temperature for Pt decorated MOFs is significantly decreased to ca. 342 °C, which could be caused by the catalytic effect of Pt under the air environment. The decomposition processes of MOFs in air can be boosted by Pt NPs. [56,57] Such phenomenon is further proved by the TGA curves obtained from different Pt loadings and different MOFs samples, as shown in Fig. S11. With the increased loadings of Pt NPs on MOFs, the lower decomposition temperature is shown. Such interactions between Pt NPs and MOFs could be further indicated by the H₂-TPR profiles presented in Fig. 2b. A significant H₂ consumption peak located at 441 °C is shown in the profile of NiNSMOFs sample, indicating the reduction process of Ni in the MOFs. For the sample of Pt NPs decorated MOFs, a broadened peak located around 226 °C is observed ascribing to the reduction of oxidized Pt species [58,59].The followed sharp peak ascribing to MOFs reduction is negatively shifted to 403 °C, which is suggestive that the Ni atoms in MOFs decorated with Pt NPs could be more chemical active compared to that of the unmodified MOFs.

To further study the electron interactions between Pt NPs and NiNSMOFs, X-ray photoelectron spectroscopy (XPS) characterization was performed on different samples and the results are shown in Fig. 3. The elemental composition is informed by the survey spectra of XPS for different samples (Fig. S12). A negative shift of 0.9 eV for Pt 4f peaks is observed on NiNSMOFs sample embedded with Pt NPs, compared to that of the as-prepared Pt NPs (Fig. 3a). This intensive decoration of electron structure for Pt could be ascribed to the modification of the ultrathin MOFs substrates. A significant positive shift of the peaks ascribed to Ni 2p is accordingly shown in the spectrum of Pt@NiNSMOFs sample (Fig. 3b), compared to pure NiMOF nanosheets. Furthermore, the content of Ni (II) in the MOF nanosheets is decreased after the

decoration of Pt NPs (Table S1). These results strongly suggest that the electrons could be partially transferred from the metal nodes in MOFs to the metal NPs embedded. Hence, the modification of the electron structure should occur on both Pt NPs and MOF nanosheets, which would intensively affect their catalytic behavior in electrochemical systems [60,61]. Similar synergistic modification effects are revealed between Pt NPs and other MOF nanosheets with different metal nodes (Fig. S13), suggesting such electron structure modification is a general phenomenon between Pt NPs and MOF nanosheets during our MOF synthesis procedure.

3.2. Electrochemical catalytic performance

The unique nano-architecture and electron interaction between Pt NPs and MOF nanosheets can result in excellent electrochemical performance towards both ORR and OER, as shown in Fig. 4. With the increase of Pt NPs loading, peaks ascribed to hydrogen absorption and desorption on Pt NPs are presented in the cyclic voltammetry (CV) curves (Fig. S13). For ORR results, it can be found from the polarization curves in Fig. 4a that all the Pt@NiNSMOFs samples with different Pt loadings have shown significantly better performance than the MOF nanosheets without Pt decoration (NiNSMOFs).

With the increase of Pt loading from 0.7 to 3.2%, the ORR activity can be remarkably enhanced with a positive onset potential shift from 0.902 to 1.024 V. However, further increase in the Pt loading to 8.8 wt % deteriorated the ORR performance. Such a volcano like catalytic performance between Pt loading and ORR activity has also been revealed in the relationship between Pt mass and specific activity (Fig. S13b). As shown in Fig. 4b, the Pt@NiNSMOFs sample (3.2 wt% of Pt) exhibits superior ORR activity to the Pt@C sample with a similar Pt loading (5 wt%). The modification effects of the MOF nanosheets with Ni as the metal node result a positive shift of 110 mV for the half-wave potential compared with that of the carbon supporting catalyst (Pt@C). The electron transfer number analyses by rotation ring-disk electrode
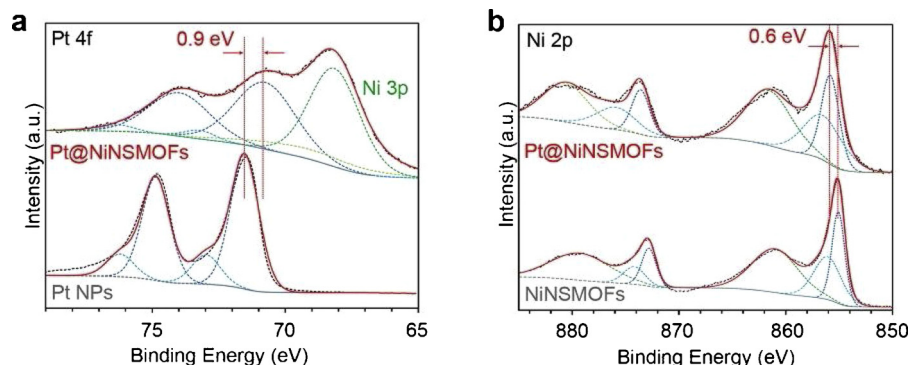

Fig. 3. Curve-fitted high resolution (a) Pt 4f and (b) Ni 2p XPS spectra of different samples.
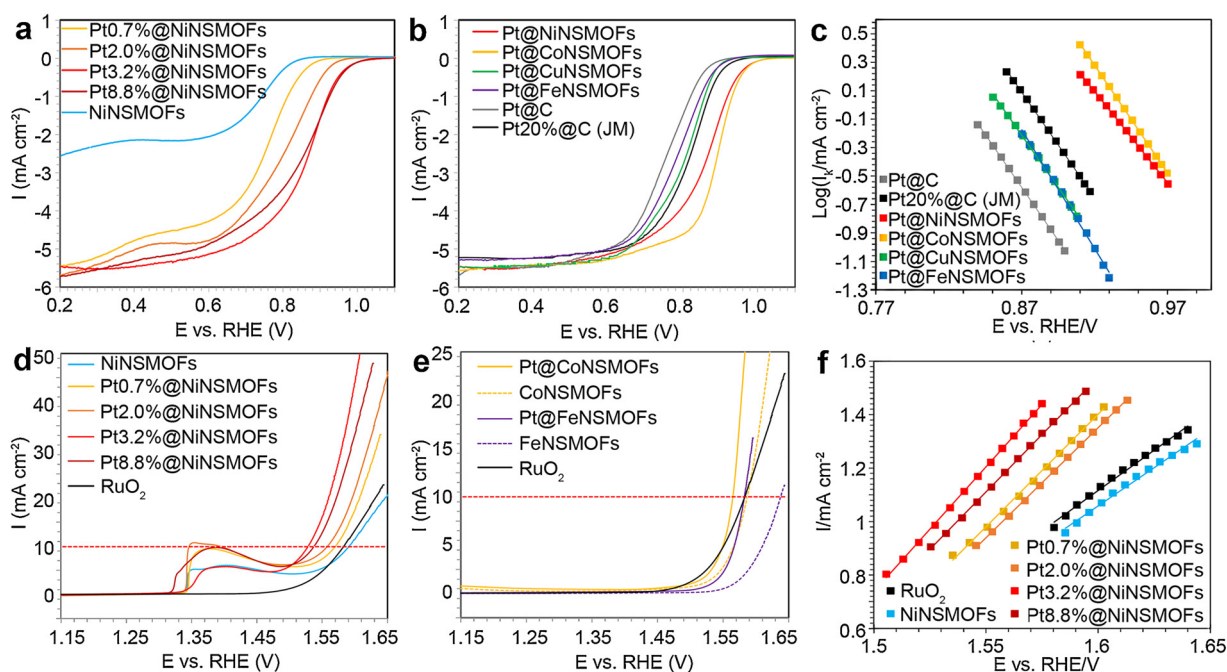
Fig. 4. Electrochemical results of different samples. (a, b) ORR polarization curves and (c) the corresponding Tafel plots at the electrolyte solution of 0.1 M KOH saturated with oxygen, at the rotation rate of 1600 rpm and the scan rate of $10\,mV\,s^{-1}$; (d, e) OER polarization curves and (f) the corresponding Tafel plots at the electrolyte solution of 0.1 M KOH saturated with oxygen, at the rotation rate of 1600 rpm and the scan rate of $10\,mV\,s^{-1}$.

(RRDE) tests and different rotation speed both confirm the direct four electron transfer mechanism within the ORR processes of Pt3.2%@NiNSMOFs catalyst (Fig. S15). Additionally, the ORR activity of a series of samples with different metal nodes was measured as well. The on-set potentials of the ORR polarization curves for all these newly designed catalysts surpass that of the Pt@C sample, which indicates the modification effects of MOF nanosheets demonstrated in the XPS results generally increase the ORR activity of Pt NPs. The samples with Ni and Co as the metal nodes exhibit remarkable performance with enhanced half-wave potentials of 48 and 75 mV compared to the commercial Pt 20%@C catalyst (Johnson Matthey, UK), respectively. Such enhancement in ORR activity for these new composite nanomaterials is also evidenced in the Tafel plots, as shown in Fig. 4c and Fig. S16. The calculated slopes (Table S3) of different Pt embedded MOF nanosheet samples are comparable to that of commercial catalyst, indicating fast dynamics of ORR process can occur on our novel electrocatalysts.

In terms of the electron decoration of Pt NPs towards MOF nanosheets to affect the OER activity, our newly designed catalysts demonstrate great enhancement as well. As shown in Fig. 4d, even pure NiMOF nanosheets exhibit close OER performance to commercial RuO$_2$ catalyst (Sigma-Aldrich). Meanwhile, a very low level of Pt loading (0.7 wt%) can significantly improve the OER activity of the pure NiMOF nanosheets, whereas the sample with 3.2 wt% Pt loading displays the optimized OER performance with a negative potential shift of 55 mV at the current density of $10\,mA\,cm^{-2}$, compared to the commercial RuO$_2$ catalyst. The modification attributed to the Pt NPs is generally validated in MOFs with different metal nodes as suggested in Fig. 4e and Fig. S17. Even though the OER performance is not comparative with the sample of Pt@NiNSMOFs, enhancement in OER activity is observed after the decoration of Pt NPs towards different MOFs. It can be seen from Fig. 4f and Fig. S18 that the Tafel plot slopes can be considerably decreased by introducing Pt NPs onto different MOF nanosheets, with the lowest value of 107 mV dec^{-1} achieved by the Pt3.2%@NiNSMOFs sample. The electrochemical results obtained from RDE tests are listed in Table S4), this catalyst design of metal NPs embedded MOF nanosheets presents superior electrochemical activity with an ultra-low over-potential gap ($E_{gap} = E_{OER10}\text{-}E_{ORR1/2}$) of 665 mV for Pt3.2%@NiNSMOFs.

To intensive understand the electrochemical properties on the active sites, chemisorption of CO pulse titration is adopted to determine the active site density ascribing to ORR and OER respectively. According to the method proposed in literature, [62] CO molecules could be chemisorbed on the sites of Pt and transition metals at $-80\,°C$. From the CO pulse chemisorption profiles presented in Fig. 5a, CO uptakes could be calculated as listed in Table S5. As the decoration of Pt NPs and the increase of the Pt loadings, CO uptakes are getting greater, indicating more active sites provided by Pt NPs. As a result, the mass-based catalytic activity for both ORR and OER is roughly increased with the growing of CO uptakes, as shown in Fig. 5b. Additionally, compared to the catalyst sample of Pt@C with a CO uptake of 330 nmol mg$_{cat.}^{-1}$, the Pt decorated MOFs samples demonstrate better ORR activity, suggesting the modification effect of MOFs towards Pt significantly enhances the catalytic performance of Pt NPs. The mass-based site density (MSD) of Pt NPs and MOFs is further calculated respectively by assuming that Pt NPs decorated on MOFs exposure similar active surface areas per particle compared to that of Pt@C, as illustrated in Fig. 5c. By subtracting the MSD provided by Pt NPs, similar densities of the active sites derived from MOFs are obtained for different Pt loading catalyst samples. Based on the MSD values for Pt NPs and MOFs, turnover frequency (TOF) for ORR and OER could be calculated respectively, as shown in Fig. 5d. For ORR situation, Pt NPs modified with MOFs exhibit superior TOF (0.22-0.39 electron site^{-1} s^{-1}) compared to carbon loaded Pt NPs (0.08 electron site^{-1} s^{-1}), whereas the increase of the Pt loadings does not significantly enhance the TOF on Pt towards ORR. On the other hand, the increase of Pt loadings on MOFs remarkably enhances the TOF on MOFs towards OER from 0.64 electron site^{-1} s^{-1} to 1.68 electron site^{-1} s^{-1}. It is reasonable that the electron decoration effects on MOFs would be intensified with the increase of Pt loadings, but not vice versa, as the contents of MOFs are in the majority of the catalyst samples. The further increase of the Pt loading results a slightly decrease of TOF towards ORR (0.22 electron site^{-1} s^{-1}), which could be caused by the agglomeration of the Pt NPs.

The synergistic effects between Pt NPs and MOF nanosheets were further analyzed via more practical analyses of the cyclic lifetime tests and rechargeable Zn-air tests. Typical responses of current density were
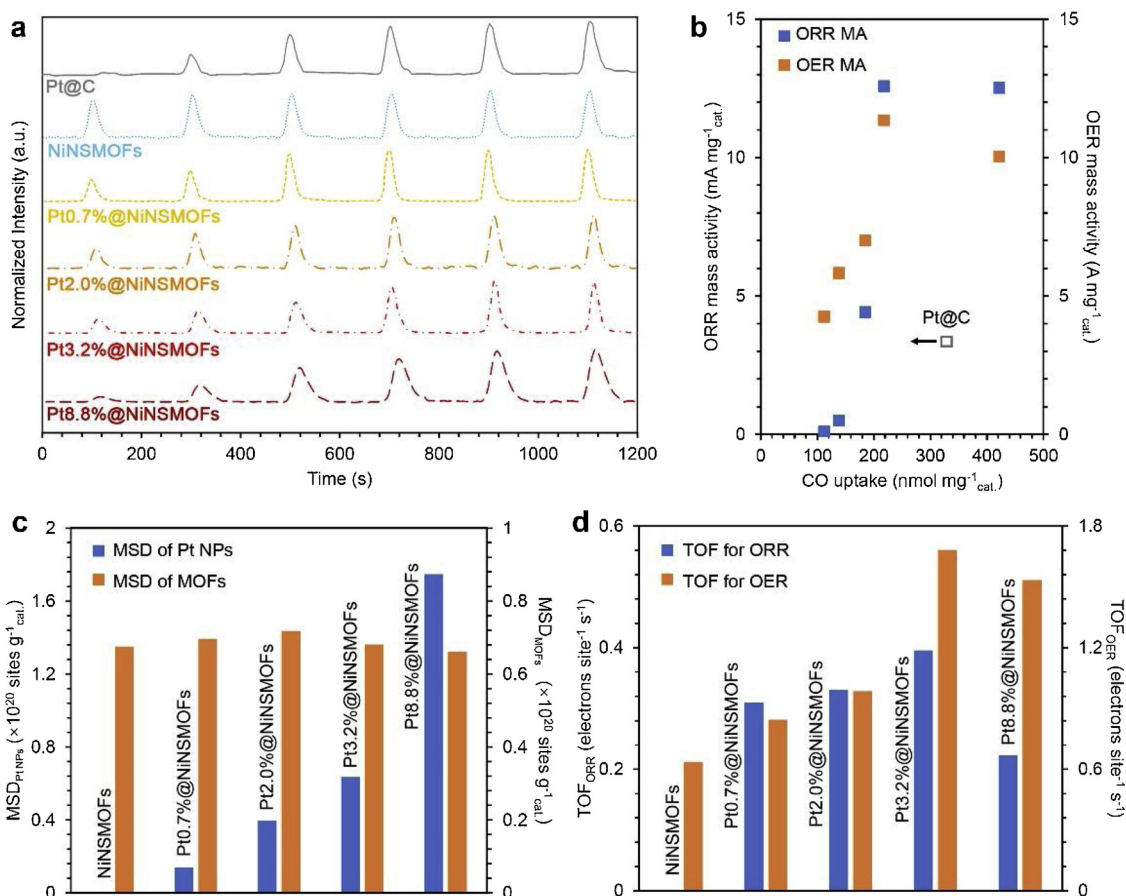
Fig. 5. Chemisorption results and electrochemical parameters. (a) CO pulse chemisorption profiles for different samples; (b) ORR (at 0.9 V vs. RHE) and OER (at 1.55 V vs. RHE) mass activity versus CO uptake obtained from different samples; (c) Mass-based site density (MSD) of Pt NPs and MOFs for different samples; (d) ORR and OER TOFs for different samples.
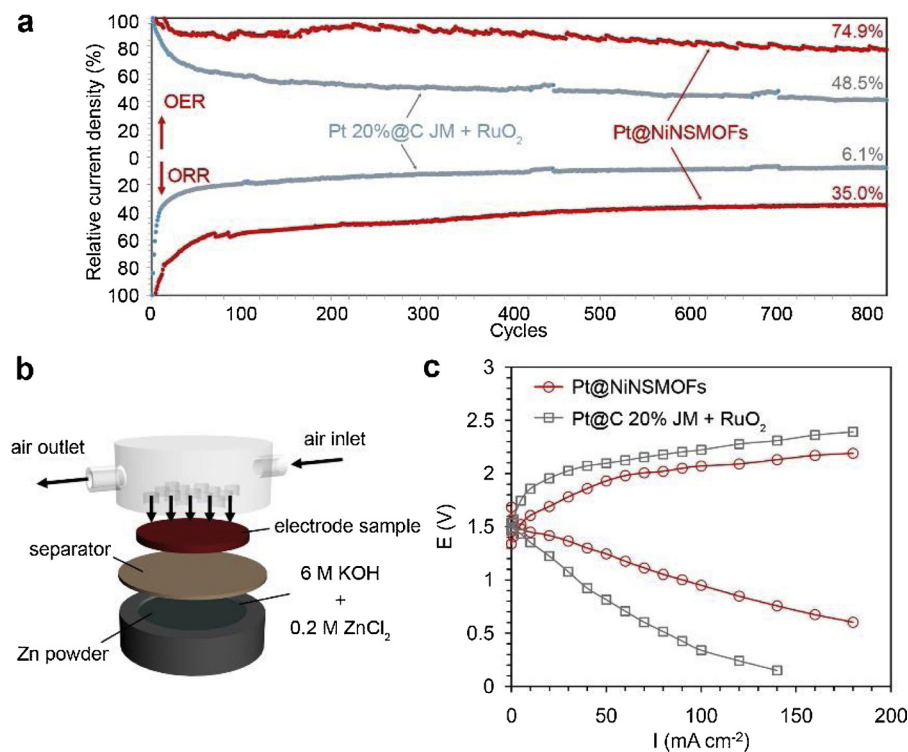

Fig. 6. (a) Cyclic lifetime test results for the electrodes coated with Pt3.2%@NiNSMOFs and commercial catalysts. The upper and lower curves demonstrate the degradation of OER and ORR performance, respectively; (b) Schematic of the fabrication of rechargeable Zn-air battery; (c) Polarization curves for charge-discharge of the rechargeable Zn-air batteries equipped with different electrodes.
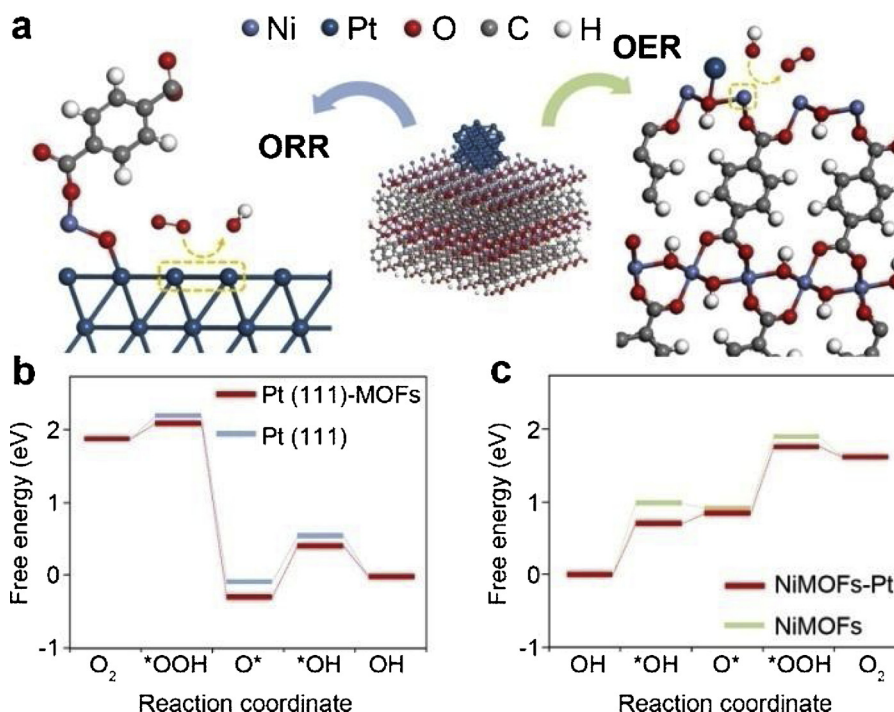
Fig. 7. (a) Schematic of the model of Pt embedded MOFs for DFT calculation; (b, c) Free energy diagrams for ORR (b) and OER (c) pathways in alkaline medium.

recorded, and the end points of the current density for every step were collected to analyze the cyclic durability of the catalyst, as shown in Fig. 6a. For the cyclic lifetime tests, the sample of Pt3.2%@NiNSMOFs was sprayed on a piece of Ni foam substrate and tested according to a cyclic potential step (0.8 and 1.55 V vs. RHE) protocol, as illustrated in Fig. S19. Obviously, the current decrease of our newly designed catalyst is much smaller compared to the electrode sprayed with the physical mixture of commercial Pt 20%@C and RuO2. After more than 800 cycles of lifetime tests towards Pt3.2%@NiNSMOFs, 74.9 and 35.0% of current density are remained for OER and ORR processes, respectively, which are much greater than 48.5 and 6.1% for that of the commercial catalysts (Fig. 6a). Such enhanced electrochemical durability is consistent with the results of the accelerated stress tests (ASTs) performed on RDE (Fig. S21).

3.3. Rechargeable Zin-air batteries tests

The superior electrochemical performance of this new catalyst design has been further proved as the air cathode catalyst in a rechargeable Zn-air battery, as illustrated in Fig. 6b (photographs of the battery assembly are shown in Fig. S22). Compared to the air cathode with commercial Pt/C and RuO2 catalysts, the polarization curves of both charge and discharge processes of the cathode using Pt3.2%@NiNS-MOFs show much better performance. The discharge and charge voltage at a low current density (10 mA cm^{-2}) is 1.450 and 1.606 V, which presents 0.097 and 0.252 V decrease in the over-potential compared to that of the commercial catalyst coated cathode. At a higher current density (100 mA cm^{-2}), the better performance is also displayed in the battery with the new catalyst, which has a discharge voltage of 0.95 V and charge voltage of 2.07 V, compared to 0.339 V and 2.222 V of the battery with the mixture of commercial Pt 20%@C and RuO2. The peak power density of the Zn-air battery with our Pt3.2%@NiNSMOFs catalyst can reach 108 mW cm^{-2}, which is 2.5-fold greater than the battery with a cathode containing commercial catalysts (Fig. S24) in both charge and discharge conditions.

3.4. DFT calculation results

Theoretical study of this newly designed composite catalyst was further carried out to elucidate the relationship between electron structural modification and catalytic activity. Calculation details using DFT can be found in the Supplementary Materials. Based on the structural features derived from the experiments and the simulation above, we constructed different simplified structures to perform the ORR and OER, respectively, as shown in Fig. 7a. The optimized stable structure and its parameters with a Pt atom anchored on the NiMOF nanosheet are illustrated in Table S6. The adsorption energy of the intermediates on the active sites is the key parameter to evaluate the catalytic performance. For the ORR pathway, a Pt (111) surface absorbed with a single metal node connected with a ligand molecule is constructed to analyze the free energy level change, as illustrated in Fig. 7a. The anchoring of the metal-organic group can lower the energy level of the intermediates during ORR and thus enhance the catalytic activity of the decorated Pt surface, as shown in the free energy profile of Fig. 7b (calculated data are shown in Table S7). The OER pathway is performed on the Ni atom adjacent to the anchored Pt atom based on previous studies of OER mechanisms on MOFs materials. Compared to the structure without Pt atom, the MOF nanosheets anchored with Pt can also weaken the adsorption strength of the intermediates on the active site (Fig. 7c and Table S8), which generates lower energy barrier and higher reaction activity for this composite catalyst.

4. Conclusion

In conclusion, we have shown that metal NPs embedded MOF nanosheets are efficient bifunctional electrochemical catalysts for energy applications. With the reciprocal modification effects on electron structures of Pt NPs and the metal nodes in MOFs, enhanced activity and durability can be achieved for both ORR and OER, and one of the lowest over-potential gaps (E$_{gap}$) of 665 mV has been achieved. The application of rechargeable Zn-air battery has solidified the practical advantages of this newly designed catalyst. The theoretical DFT calculation confirms that the activity enhancement on Pt and MOFs towards ORR and OER, respectively, derives from the decoration of the

two materials towards each other. This new strategy can not only provide new nano-architecture for multiple energy applications, such as fuel cells, secondary metal-air batteries, and water splitting devices, but also shed lights on the design for new catalysts, synthesis of advanced energy materials, and construction of novel electrochemical devices.

Appendix A. Supplementary data

Supplementary material related to this article can be found, in the online version, at doi:https://doi.org/10.1016/j.apcatb.2018.12.073.

References

[1] F. Cheng, J. Chen, Metal-air batteries: from oxygen reduction electrochemistry to cathode catalysts, Chem. Soc. Rev. 41 (2012) 2172–2192.
[2] M.K. Debe, Electrocatalyst approaches and challenges for automotive fuel cells, Nature 486 (2012) 43–51.
[3] N.-T. Suen, S.-F. Hung, Q. Quan, N. Zhang, Y.-J. Xu, H.M. Chen, Electrocatalysis for the oxygen evolution reaction: recent development and future perspectives, Chem. Soc. Rev. 46 (2017) 337–365.
[4] E. Davari, D.G. Ivey, Bifunctional electrocatalysts for Zn-air batteries, Sustain. Energy Fuel 2 (2018) 39–67.
[5] Y. Gorlin, T.F. Jaramillo, A bifunctional nonprecious metal catalyst for oxygen reduction and water oxidation, J. Am. Chem. Soc. 132 (2010) 13612–13614.
[6] Z.-F. Huang, J. Wang, Y. Peng, C.-Y. Jung, A. Fisher, X. Wang, Design of efficient bifunctional oxygen Reduction/Evolution electrocatalyst: recent advances and perspectives, Adv. Energy Mater. 7 (2017).
[7] M. Kuang, G. Zheng, Nanostructured bifunctional redox electrocatalysts, Small 12 (2016) 5656–5675.
[8] J. Zhang, Z. Zhao, Z. Xia, L. Dai, A metal-free bifunctional electrocatalyst for oxygen reduction and oxygen evolution reactions, Nat. Nanotechnol. 10 (2015) 444–452.
[9] V.R. Stamenkovic, B.S. Mun, M. Arenz, K.J.J. Mayrhofer, C.A. Lucas, G. Wang, P.N. Ross, N.M. Markovic, Trends in electrocatalysis on extended and nanoscale Pt-bimetallic alloy surfaces, Nat. Mater. 6 (2007) 241–247.
[10] E. Antolini, Iridium as catalyst and cocatalyst for oxygen Evolution/Reduction in acidic polymer electrolyte membrane electrolyzers and fuel cells, ACS Catal. 4 (2014) 1426–1440.
[11] G.-R. Zhang, S. Woellner, Hollowed structured PtNi bifunctional electrocatalyst with record low total overpotential for oxygen reduction and oxygen evolution reactions, Appl. Catal. B Environ. 222 (2018) 26–34.
[12] Y. Liang, Y. Li, H. Wang, J. Zhou, J. Wang, T. Regier, H. Dai, Co3O4 nanocrystals on graphene as a synergistic catalyst for oxygen reduction reaction, Nat. Mater. 10 (2011) 780–786.
[13] A. Aijaz, J. Masa, C. Roesler, W. Xia, P. Weide, A.J.R. Botz, R.A. Fischer, W. Schuhmann, M. Muhler, Co@Co3O4 encapsulated in carbon nanotube-grafted nitrogen-doped carbon polyhedra as an advanced bifunctional oxygen electrode, Angew. Chem. Int. Ed. 55 (2016) 4087–4091.
[14] J. Suntivich, K.J. May, H.A. Gasteiger, J.B. Goodenough, Y. Shao-Horn, A perovskite oxide optimized for oxygen evolution catalysis from molecular orbital principles, Science 334 (2011) 1383–1385.
[15] B. Kang, X. Jin, S.M. Oh, S.B. Patil, M.G. Kim, S.H. Kim, S.-J. Hwang, An effective way to improve bifunctional electrocatalyst activity of manganese oxide via control of bond competition, Appl. Catal. B Environ. 236 (2018) 107–116.
[16] G. Wu, A. Santandreu, W. Kellogg, S. Gupta, O. Ogoke, H. Zhang, H.-L. Wang, L. Dai, Carbon nanocomposite catalysts for oxygen reduction and evolution reactions: from nitrogen doping to transition-metal addition, Nano Energy 29 (2016) 83–110.
[17] Y. Xu, M. Kraft, R. Xu, Metal-free carbonaceous electrocatalysts and photocatalysts for water splitting, Chem. Soc. Rev. 45 (2016) 3039–3052.
[18] K. Mamtani, D. Jain, D. Dogu, V. Gustin, S. Gunduz, A.C. Co, U.S. Ozkan, Insights into oxygen reduction reaction (ORR) and oxygen evolution reaction (OER) active sites for nitrogen-doped carbon nanostructures (CNx) in acidic media, Appl. Catal. B Environ. 220 (2018) 88–97.
[19] A. Arul, H. Pak, K.U. Moon, M. Christy, M.Y. Oh, K.S. Nahm, Metallomacrocyclic carbon complex: a study of bifunctional electrocatalytic activity for oxygen reduction and oxygen evolution reactions and their lithium-oxygen battery applications, Appl. Catal. B Environ. 220 (2018) 488–496.
[20] H.-C. Zhou, J.R. Long, O.M. Yaghi, Introduction to metal-organic frameworks, Chem. Rev. 112 (2012) 673–674.
[21] H. Furukawa, K.E. Cordova, M. O'Keeffe, O.M. Yaghi, The chemistry and applications of metal-organic frameworks, Science 341 (2013) 1230444.
[22] J.-R. Li, J. Sculley, H.C. Zhou, Metal-organic frameworks for separations, Chem. Rev. 112 (2012) 869–932.
[23] L.J. Murray, M. Dinca, J.R. Long, Hydrogen storage in metal-organic frameworks, Chem. Soc. Rev. 38 (2009) 1294–1314.
[24] P. Horcajada, R. Gref, T. Baati, P.K. Allan, G. Maurin, G. Ferey, R.E. Morris, C. Serre, Metal-organic frameworks in biomedicine, Chem. Rev. 112 (2012) 1232–1268.
[25] P. Horcajada, T. Chalati, C. Serre, B. Gillet, C. Sebrie, T. Baati, J.F. Eubank, D. Heurtaux, P. Clayette, C. Kreuz, J.-S. Chang, Y.K. Hwang, V. Marsaud, P.-N. Bories, L. Cynober, S. Gil, G. Ferey, P. Couvreur, R. Gref, Porous metal-organic-framework nanoscale carriers as a potential platform for drug delivery and imaging, Nat. Mater. 9 (2010) 172–178.
[26] A. Foucault-Collet, K.A. Gogick, K.A. White, S. Villette, A. Pallier, G. Collet, C. Kieda, T. Li, S.J. Geib, N.L. Rosi, S. Petoud, Lanthanide near infrared imaging in living cells with Yb3+ nano metal organic frameworks, Proc. Natl. Acad. Sci. U. S. A. 110 (2013) 17199–17204.
[27] Y. Cui, Y. Yue, G. Qian, B. Chen, Luminescent functional metal-organic frameworks, Chem. Rev. 112 (2012) 1126–1162.
[28] L.E. Kreno, K. Leong, O.K. Farha, M. Allendorf, R.P. Van Duyne, J.T. Hupp, Metal-organic framework materials as chemical sensors, Chem. Rev. 112 (2012) 1105–1125.
[29] D. Farrusseng, S. Aguado, C. Pinel, Metal-organic frameworks: opportunities for catalysis, Angew. Chem. Int. Ed. 48 (2009) 7502–7513.
[30] J. Lee, O.K. Farha, J. Roberts, K.A. Scheidt, S.T. Nguyen, J.T. Hupp, Metal-organic framework materials as catalysts, Chem. Soc. Rev. 38 (2009) 1450–1459.
[31] S. Inagaki, S. Guan, T. Ohsuna, O. Terasaki, An ordered mesoporous organosilica hybrid material with a crystal-like wall structure, Nature 416 (2002) 304–307.
[32] H.-L. Jiang, Y. Tatsu, Z.-H. Lu, Q. Xu, Non-, Micro-, and mesoporous metal-organic framework isomers: reversible transformation, fluorescence sensing, and large molecule separation, J. Am. Chem. Soc. 132 (2010) 5586–5587.
[33] F. Schuth, W. Schmidt, Microporous and mesoporous materials, Adv. Mater. 14 (2002) 629–638.
[34] H. Furukawa, N. Ko, Y.B. Go, N. Aratani, S.B. Choi, E. Choi, A.O. Yazaydin, R.Q. Snurr, M. O'Keeffe, J. Kim, O.M. Yaghi, Ultrahigh porosity in metal-organic frameworks, Science 329 (2010) 424–428.
[35] B.Y. Xia, Y. Yan, N. Li, H.B. Wu, X.W. Lou, X. Wang, A metal-organic framework-derived bifunctional oxygen electrocatalyst, Nat. Energy 1 (2016).
[36] J. Ying, J. Li, G. Jiang, Z.P. Cano, Z. Ma, C. Zhong, D. Su, Z. Chen, Metal-organic frameworks derived platinum-cobalt bimetallic nanoparticles in nitrogen-doped hollow porous carbon capsules as a highly active and durable catalyst for oxygen reduction reaction, Appl. Catal. B Environ. 225 (2018) 496–503.
[37] H.-L. Jiang, B. Liu, Y.-Q. Lan, K. Kuratani, T. Akita, H. Shioyama, F. Zong, Q. Xu, From metal-organic framework to nanoporous carbon: toward a very high surface area and hydrogen uptake, J. Am. Chem. Soc. 133 (2011) 11854–11857.
[38] D. Zhu, C. Guo, J. Liu, L. Wang, Y. Du, S.-Z. Qiao, Two-dimensional metal-organic frameworks with high oxidation states for efficient electrocatalytic urea oxidation, Chem. Comm. 53 (2017) 10906–10909.
[39] S.L. Zhao, Y. Wang, J.C. Dong, C.T. He, H.J. Yin, P.F. An, K. Zhao, X.F. Zhang, C. Gao, L.J. Zhang, J.W. Lv, J.X. Wang, J.Q. Zhang, A.M. Khattak, N.A. Khan, Z.X. Wei, J. Zhang, S.Q. Liu, H.J. Zhao, Z.Y. Tang, Ultrathin metal-organic framework nanosheets for electrocatalytic oxygen evolution, Nat. Energy 1 (2016) 1–10.
[40] C.L. Tan, X.H. Cao, X.J. Wu, Q.Y. He, J. Yang, X. Zhang, J.Z. Chen, W. Zhao, S.K. Han, G.H. Nam, M. Sindoro, H. Zhang, Recent advances in ultrathin two-dimensional nanomaterials, Chem. Rev. 117 (2017) 6225–6331.
[41] J. Yu, C. Mu, B. Yan, X. Qin, C. Shen, H. Xue, H. Pang, Nanoparticle/MOF composites: preparations and applications, Mater. Horizons 4 (2017) 557–569.
[42] M. Zhao, K. Yuan, Y. Wang, G. Li, J. Guo, L. Gu, W. Hu, H. Zhao, Z. Tang, Metal-organic frameworks as selectivity regulators for hydrogenation reactions, Nature 539 (2016) 76–80.
[43] Q. Yang, Q. Xu, H.-L. Jiang, Metal-organic frameworks meet metal nanoparticles: synergistic effect for enhanced catalysis, Chem. Soc. Rev. 46 (2017) 4774–4808.
[44] K. Kamiya, R. Kamai, K. Hashimoto, S. Nakanishi, Platinum-modified covalent triazine frameworks hybridized with carbon nanoparticles as methanol-tolerant oxygen reduction electrocatalysts, Nat. Commun. 5 (2014).
[45] W. Xia, R. Zou, L. An, D. Xia, S. Guo, A metal-organic framework route to in situ encapsulation of Co@Co3O4@C core@bishell nanoparticles into a highly ordered porous carbon matrix for oxygen reduction, Energy Environ. Sci. 8 (2015) 568–576.
[46] S. Dou, C.-L. Dong, Z. Hu, Y.-C. Huang, J.-L. Chen, L. Tao, D. Yan, D. Chen, S. Shen, S. Chou, S. Wang, Atomic-scale CoOx species in metal-organic frameworks for oxygen evolution reaction, Adv. Funct. Mater. 27 (2017).
[47] W. Zhou, J. Lu, K. Zhou, L. Yang, Y. Ke, Z. Tang, S. Chen, CoSe2 nanoparticles embedded defective carbon nanotubes derived from MOFs as efficient electrocatalyst for hydrogen evolution reaction, Nano Energy 28 (2016) 143–150.
[48] J. Lu, W. Zhou, L. Wang, J. Jia, Y. Ke, L. Yang, K. Zhou, X. Liu, Z. Tang, L. Li, S. Chen, Core-shell nanocomposites based on gold Nanoparticle@Zinc-Iron-Embedded porous carbons derived from metal-organic frameworks as efficient dual catalysts for oxygen reduction and hydrogen evolution reactions, ACS Catal. 6 (2016) 1045–1053.
[49] Y. Liang, J. Wei, X. Zhang, J. Zhang, S.P. Jiang, H. Wang, Synthesis of nitrogen-doped porous carbon nanocubes as a catalyst support for methanol oxidation,

Chemcatchem 8 (2016) 1901–1904.

[50] Y. Zhao, J. Zhang, J. Song, J. Li, J. Liu, T. Wu, P. Zhang, B. Han, Ru nanoparticles immobilized on metal-organic framework nanorods by supercritical CO2-methanol solution: highly efficient catalyst, Green Chem. 13 (2011) 2078–2082.

[51] R. Hinogami, S. Yotsuhashi, M. Deguchi, Y. Zenitani, H. Hashiba, Y. Yamada, Electrochemical reduction of carbon dioxide using a copper rubeanate metal organic framework, ECS Electrochem. Lett. 1 (2012) H17–H19.

[52] L. Shi, T. Wang, H. Zhang, K. Chang, J. Ye, Electrostatic self-assembly of nanosized carbon nitride nanosheet onto a zirconium metal-organic framework for enhanced photocatalytic CO2 reduction, Adv. Funct. Mater. 25 (2015) 5360–5367.

[53] Z. Zhou, S. Wang, W. Zhou, G. Wang, L. Jiang, W. Li, S. Song, J. Liu, G. Sun, Q. Xin, Novel synthesis of highly active Pt/C cathode electrocatalyst for direct methanol fuel cell, Chem. Comm. (2003) 394–395.

[54] J.J. Duan, S. Chen, C. Zhao, Ultrathin metal-organic framework array for efficient electrocatalytic water splitting, Nat. Commun. 8 (2017).

[55] H.B. Yang, J. Miao, S.-F. Hung, J. Chen, H.B. Tao, X. Wang, L. Zhang, R. Chen, J. Gao, H.M. Chen, L. Dai, B. Liu, Identification of catalytic sites for oxygen reduction and oxygen evolution in N-doped graphene materials: development of highly efficient metal-free bifunctional electrocatalyst, Sci. Adv. 2 (2016).

[56] P. Bazin, O. Saur, F.C. Meunier, M. Daturi, J.C. Lavalley, A.M. Le Govic, V. Harle, G. Blanchard, A thermogravimetric and FT-IR study of the reduction by H-2 of

[57] M.R.Z. Ghavidel, E.B. Easton, Thermally induced changes in the structure and ethanol oxidation activity of Pt0.25Mn0.75/C, Appl. Catal. B Environ. 176 (2015) 150–159.

[58] R. Crisafulli, V.V.S. de Barros, F.E. Rodrigues de Oliveira, T. de Araújo Rocha, S. Zignani, L. Spadaro, A. Palella, J.A. Dias, J.J. Linares, On the promotional effect of Cu on Pt for hydrazine electrooxidation in alkaline medium, Appl. Catal. B Environ. 236 (2018) 36–44.

[59] H.W. Huang, R.R. Cao, S.X. Yu, K. Xu, W.C. Hao, Y.G. Wang, F. Dong, T.R. Zhang, Y.H. Zhang, Single-unit-cell layer established Bi2WO6 3D hierarchical architectures: efficient adsorption, photocatalysis and dye-sensitized photoelectrochemical performance, Appl. Catal. B Environ. 219 (2017) 526–537.

[60] Z. Xia, S. Wang, L. Jiang, H. Sun, S. Liu, X. Fu, B. Zhang, D.S. Su, J. Wang, G. Sun, Bio-inspired construction of advanced fuel cell cathode with Pt anchored in ordered hybrid polymer matrix, Sci. Rep. 5 (2015).

[61] S. Chen, Z. Wei, X. Qi, L. Dong, Y.-G. Guo, L. Wan, Z. Shao, L. Li, Nanostructured polyaniline-decorated Pt/C@PANI core-shell catalyst with enhanced durability and activity, J. Am. Chem. Soc. 134 (2012) 13252–13255.

[62] N.R. Sahraie, U.I. Kramm, J. Steinberg, Y. Zhang, A. Thomas, T. Reier, J.-P. Paraknowitsch, P. Strasser, Quantifying the density and utilization of active sites in non-precious metal oxygen electroreduction catalysts, Nat. Commun. 6 (2015).

sulfated Pt/CexZr1-xO2 solids, Appl. Catal. B Environ. 90 (2009) 368–379.